Electronic Supplementary Material (ESI) for Journal of Materials Chemistry C.
This journal is © The Royal Society of Chemistry 2023

Supplementary Information

Moderate Temperature Sulfurization and Selenization of Highly Stable Metal Oxides: An Opportunity for Chalcogenide Perovskites

Shubhanshu Agarwal‡, Jonathan W. Turnley‡, Apurva A. Pradhan, Rakesh Agrawal*

Davidson School of Chemical Engineering, Purdue University, West Lafayette, Indiana 47907, United States

‡ These authors contributed equally.

* Rakesh Agrawal – Davidson School of Chemical Engineering, Purdue University, West Lafayette, Indiana 47907, United States
Email: agrawalr@purdue.edu

Experimental Methods

Calculations

The Gibbs energy of a reaction as a function of temperature was determined by the sum of the Gibbs formation energies as a function of temperature of the products minus the sum of the Gibbs formation energies as a function of temperature of the reactants.

$$\Delta G^{o}_{rxn}(T) = \sum n * \Delta_f G^{o}_{products}(T) - \sum m * \Delta_f G^{o}_{reactants}(T)$$

In the previous equation, n and m represent the coefficients of the products and reactants for the equation that defines the chemical reaction of interest. The Gibbs formation energy as a function of temperature was determined considering the standard formation enthalpy and entropy at 298 K and accounting for changes to the enthalpy and entropy at different temperatures, assuming the heat capacity determined at 298 K is a constant across this temperature range.

$$\Delta_f G^o(T) = \Delta_f H^o + C_p \int_{298}^{T} dT \; - T(S^o + C_p \int_{298}^{T} \frac{1}{T} dT)$$

The standard formation enthalpies, entropies, and heat capacities were obtained from literature and are listed below in Table S1.[1–4] Where heat capacity was not available, the Neumann-Kopp approximation was used to make an estimate.[5,6] This method is discussed below and results are shown in Table S2.

The temperature dependent reaction equilibrium constant, K_{eq}, was then calculated based on the Gibbs energy of the reaction.

$$\ln\left(K_{eq}\right) = \frac{-\Delta G^{o}_{rxn}(T)}{RT}$$

Materials

Polyvinyl butyral, sulfur flakes (99.99%), alumina dispersed in IPA (20 wt%), propionic acid (ACS Reagent, >99.5%), and 2-Propanol (99.5%, anhydrous) were purchased from Sigma Aldrich. Methanol (HPLC grade) and ethanol (HPLC grade) were purchased from Fisher. Zirconium(IV) chloride (98%, anhydrous) and $SrZrO_3$ powder (99.3%) were purchased from Thermo Scientific. Barium acetate (99%) and zirconium acetylacetonate (97%) were purchased from STREM. Hafnium hydride nanopowder (99.9%, APS < 100 nm), zirconium hydride nanopowder (99.9%, APS < 100 nm), and Titanium hydride nanopowder (99.5%, APS < 100 nm) were purchased from Nano Research Elements. Hafnium disulfide (>99.995%) was purchased from Ossila. Corning Eagle XG glass was purchased from Stemmerich. Quartz slides were purchased from Quartz Scientific. Sulfur was ground with a mortar and pestle and dried under vacuum overnight. All other chemicals were used as received.

Safety Considerations for Metal Hydrides

As has been previously reported, metal hydrides such as TiH_2, ZrH_2, and HfH_2 are considered flammable solids and care should be taken to prevent runaway reactions with oxygen or water.[7,8] This is especially true when using a nanopowder that could form a flammable or explosive dust. Metal hydrides in this work were stored and handled in a nitrogen-filled glovebox or in a vessel connected to an argon-filled Schlenk line. Small amounts of metal hydrides were used in any given reaction to minimize hazards.

Methods

Alumina-coated substrates were prepared via spin coating on cleaned substrates. Eagle XG glass was cleaned by rinsing with 2-propanol and methanol, sonicating in an Alconox solution, sonicating in ultrapure water, and finally UV-ozone treatment. Quartz substrates were cleaned by rinsing with 2-propanol, methanol, and ultrapure water before UV-ozone treatment. The as-purchased Al_2O_3 solution was diluted 10 times with IPA. Then a thin alumina layer was coated on the cleaned substrates using a spin coater with 1000 rpm for 1 min. The Al_2O_3-coated substrates were then heated to 500°C for 30 min in air.

Zirconium oxide films were solution deposited onto Al_2O_3-coated Eagle XG glass substrates. The ink consisted of a 0.3 M solution of $ZrCl_4$ in ethanol. The ink was spin coated in air at 1000 rpm for 1 min. The film was then dried at 100 °C for 1 min in air. To produce an amorphous ZrO_2 film, the temperature was ramped up to 300 °C (which roughly took 3 min 50 s) and kept at 300 °C for 2 min. To produce a crystalline ZrO_2 sample, following the 100 °C step the temperature was ramped to 500 °C (which roughly took 7 min 30 s) and kept at 500 °C for 1 min. The sample was then loaded into an air-exposed tube furnace and heated to 500 °C for 12 h.

$BaZrO_3$ films were solution deposited onto Al_2O_3-coated quartz substrates based on the method by Gupta et al.[9] Inks were 0.3 M in barium acetate and 0.3 M in zirconium acetylacetonate with propionic acid as the solvent. Additionally, 0.5 g of polyvinyl butyral was added per 15 mL of solution. Dissolution was done at 60 °C for 1 h. The ink was then spin coated at 2000 rpm for 1 min and then 5000 rpm for 5 min. The film was then annealed at 500 °C for 5 min. This coating and annealing cycle was performed 10 times. Finally, the film was heated at 700 °C for 12 h to produce crystalline $BaZrO_3$.

In a standard chalcogenization, 0.05 mmol of the metal hydride sink (HfH_2, ZrH_2, TiH_2) and 10 mg of S powder or 15 mg of Se powder were added to a small borosilicate tube. The small borosilicate tube and the metal oxide film (ZrO_2 or $BaZrO_3$) or metal oxide powder ($SrZrO_3$) were then loaded into a 5 mL borosilicate ampule and sealed under vacuum with an argon pressure below 200 mtorr. The ampule was then loaded into a tube furnace and heated. For the chalcogenization of ZrO_2 samples, a temperature of 500 °C was used. For the chalcogenization of $BaZrO_3$ or $SrZrO_3$ samples, a temperature of 575 °C was used.

Characterization

Powder X-ray Diffraction (XRD) was done using a Rigaku SmartLab diffractometer operated at 40 kV/44 mA in parallel beam mode with a Cu Kα (λ = 1.5406 Å) source. Raman spectroscopy was done with a Horiba/Jobin-Yvon HR800 Raman spectrometer using a 632.8 nm excitation laser wavelength. Scanning electron microscopy (SEM) and energy dispersive X-ray (EDX) analyses were conducted using a Quanta 3D FEG with an accelerating voltage of 20 kV, a

spot size of 1.0, and a working distance of 10 mm unless otherwise mentioned.

Supplementary Results and Discussion

Table S1: Thermodynamic Properties of Relevant Materials

Compound	$\Delta_f H^0$ (kJ/mol)	S^0 (J/mol*K)	C_p (J/mol*K)	Source
ZrO_2 (crystalline)	-1100.6	50.4	56.2	[1]
ZrS_2 (crystalline)	-573.2	78.2	56.4	[2]
ZrS_3 (crystalline)	-615.2	90.7		[2]
HfO_2 (crystalline)	-1144.7	59.3	60.3	[1]
HfS_2 (crystalline)	-585.8	83.7	51.4	[3,4]
HfS_3 (crystalline)	-623.4	96.2		[3]
TiO_2 (crystalline)	-944.0	50.6	40.0	[1]
TiS_2 (crystalline)	-407.1	78.2	67.9	[3]
TiS_3 (crystalline)	-429.7	90.8		[3]
O_2 (gaseous)	0.0	205.2	29.4	[1]
S_8 (gaseous)	99.6	423.1	173.9	[3]
S (crystalline)	0.0	31.9	22.8	[3]
C (crystalline)	0.0	5.7	8.5	[1]
CO (gaseous)	-110.5	197.7	29.1	[1]
CO_2 (gaseous)	-393.5	213.8	37.1	[1]
CS_2 (gaseous)	116.7	237.8	45.4	[1]
H_2 (gaseous)	0.0	130.7	28.8	[1]
H_2O (gaseous)	-241.8	188.8	33.6	[1]
H_2S (gaseous)	-20.6	205.8	34.2	[1]

Supplemental Discussion 1. Neumann-Kopp Approximation of Heat Capacity (C_p)

The Neumann-Kopp rule for approximating heat capacities estimates that the heat capacity contributions per atom remain constant. Therefore, the heat capacity for a solid multinary material can be estimated if the heat capacities from the solid form of its pure elemental constituents are known.[5] So for a material $A_aB_bC_c$ the molar heat capacity is estimated by:

$$C_p(A_aB_bC_c) = aC_p(A) + bC_p(B) + cC_p(C)$$

The Neumann-Kopp rule has been shown to be a reasonable estimate for room-temperature heat capacities. However, Leitner et al. altered the Neumann-Kopp estimation by using values for binary oxides to estimate ternary oxides.[6] In this line of thinking, we can estimate the molar heat capacities of the transition metal trichalcogenides, AX_3, by the sum of the contributions from the transition metal dichalcogenides, AX_2, and the chalcogen, X.

$$C_p(AX_3) = C_p(AX_2) + C_p(X)$$

Table S2. Approximation of Transition Metal Trichalcogenide Heat Capacities

Compound	Neumann-Kopp Approximation of C_p (J/mol*K)
TiS_3	90.7
ZrS_3	79.2
HfS_3	74.2

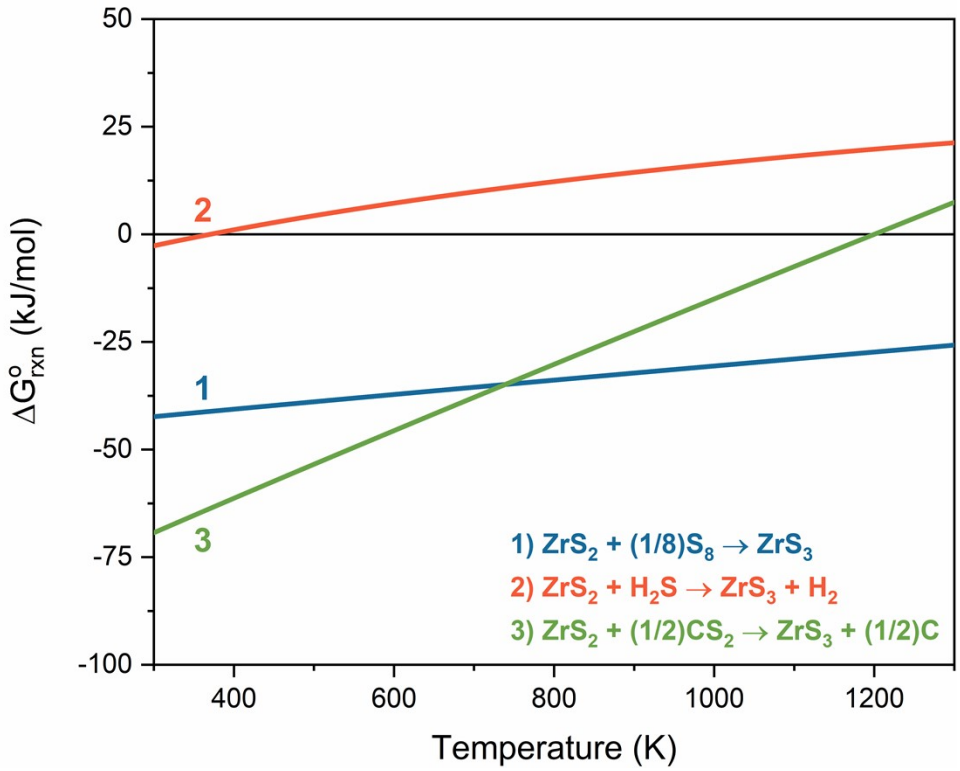

Figure S1. Gibbs Energy of the reaction as a function of temperature considering the formation of ZrS_2 or ZrS_3 in the presence of a sulfur source. Note that at very high temperatures, CS_2 can dissociate into radicals so experimental observations may differ from these thermodynamic calculations shown here.[10]

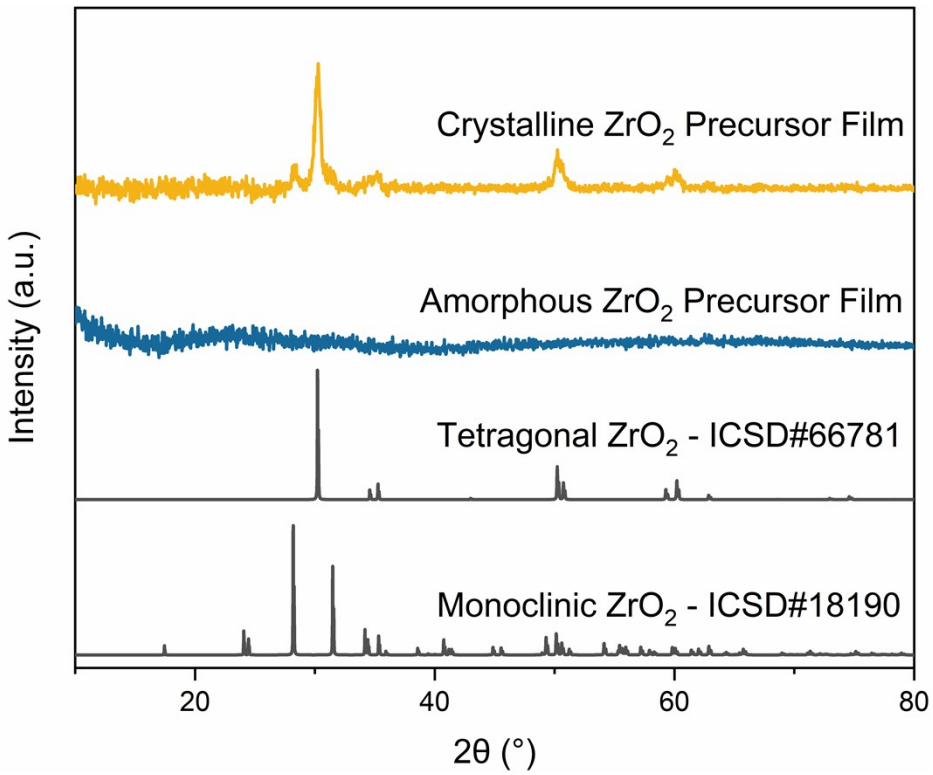

Figure S2. XRD pattern for the solution-processed ZrO_2 precursor films used in this study. Following the initial heat treatment, the films were amorphous. However, crystalline ZrO_2 was obtained as a mixture of the tetragonal and monoclinic phases upon further heating.

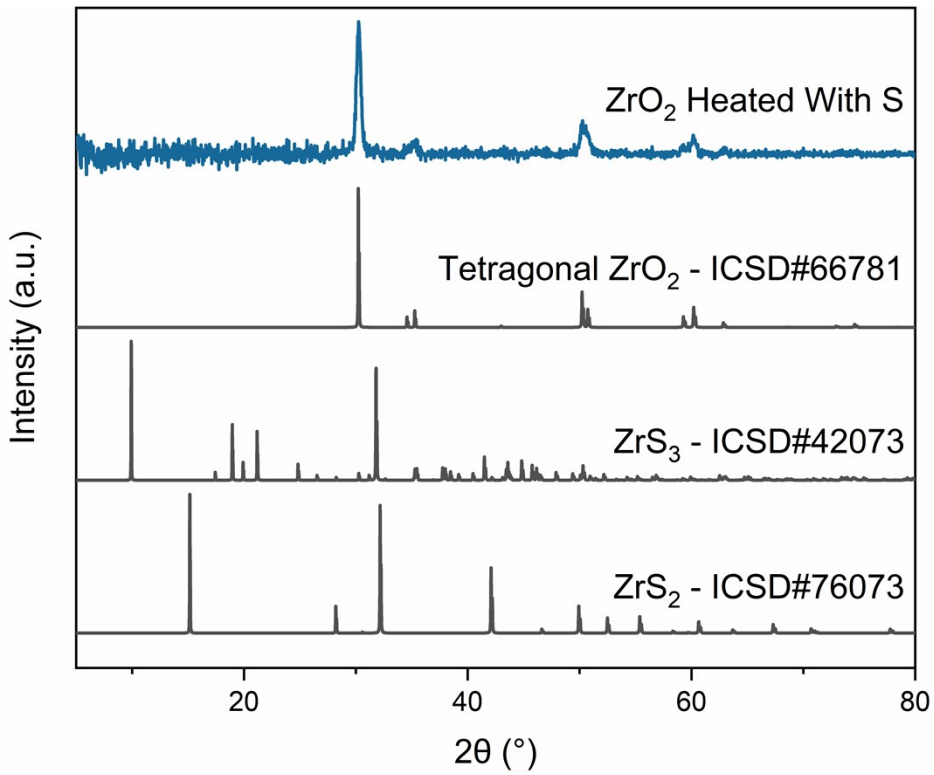

Figure S3. XRD pattern for an amorphous ZrO_2 precursor film that was heated in an evacuated ampule with S powder at 500 °C for 24 h. Sulfur could not convert the film to a zirconium sulfide and instead the amorphous ZrO_2 precursor formed crystalline ZrO_2 during the heating. Note that the lack of monoclinic ZrO_2 is likely due to the longer heating time.

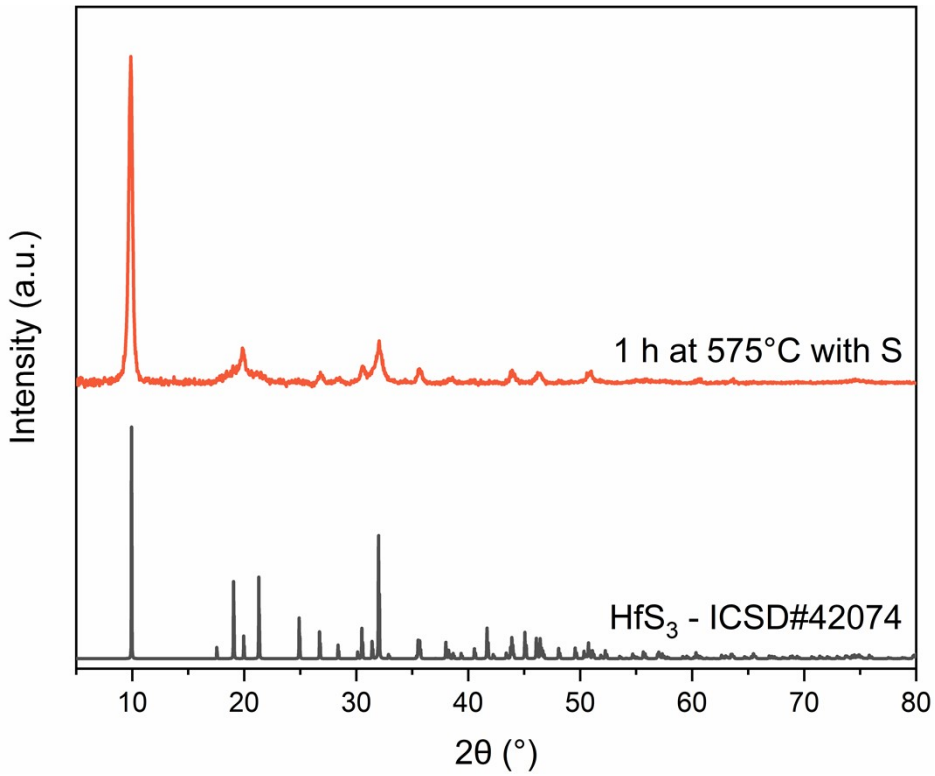

Figure S4. XRD pattern for the HfH_2 sink after it has been heated in the presence of sulfur for 1 h at 575 °C and converted to HfS_3.

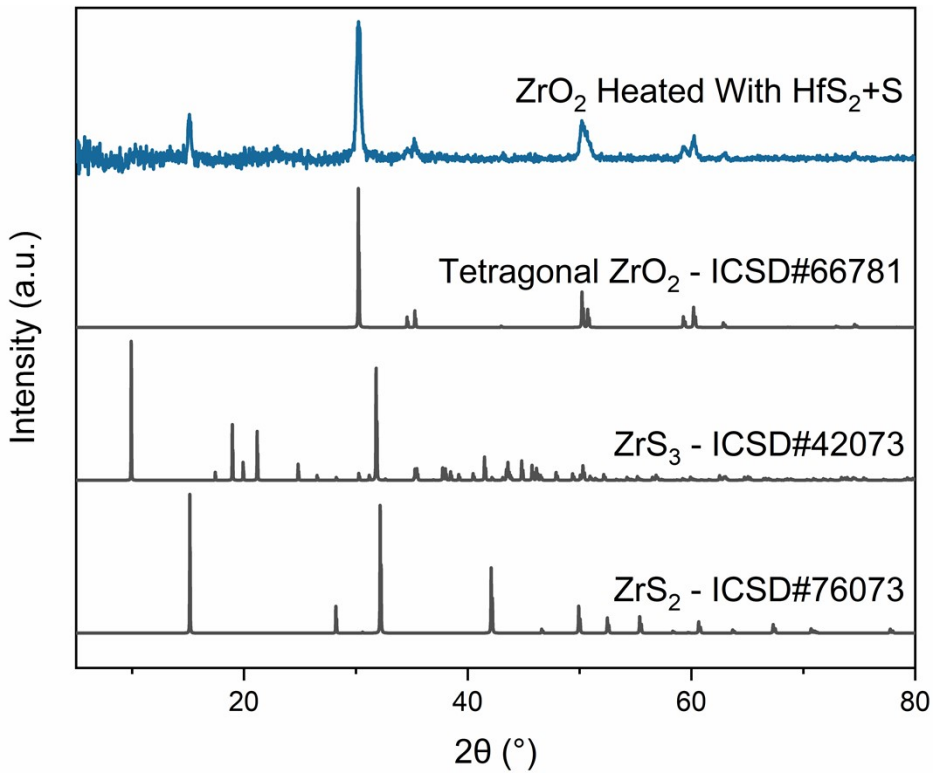

Figure S5. XRD pattern for an amorphous ZrO_2 precursor film that was heated in an evacuated ampule with HfS_2 and S powder at 500 °C for 48 h. Most peaks can be mapped to the ZrO_2 reference, with one peak indicating the presence of some ZrS_2.

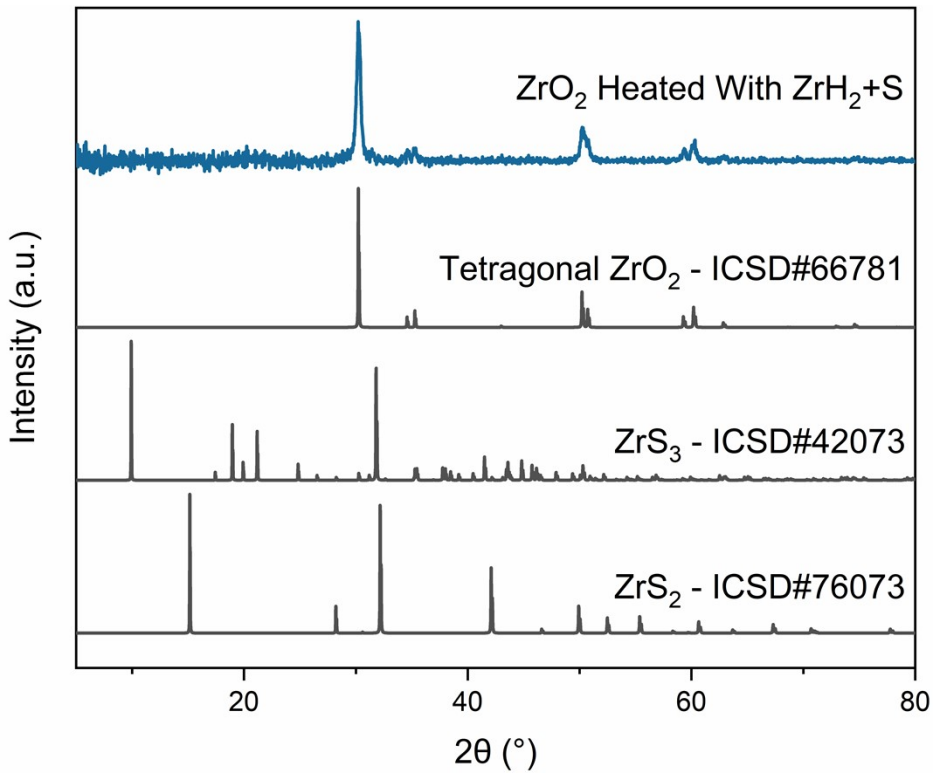

Figure S6. XRD pattern for an amorphous ZrO_2 precursor film that was heated in an evacuated ampule with ZrH_2 and S powder at 500 °C for 24 h. All peaks can be mapped to the ZrO_2 reference.

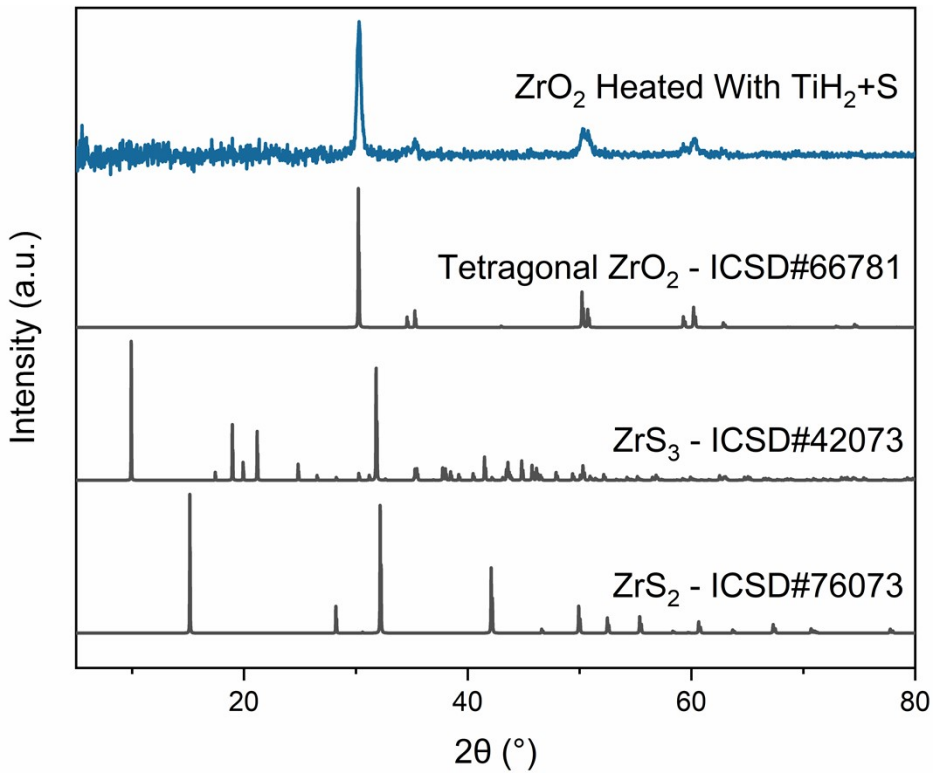

Figure S7. XRD pattern for an amorphous ZrO_2 precursor film that was heated in an evacuated ampule with TiH_2 and S powder at 500 °C for 24 h. All peaks can be mapped to the ZrO_2 reference.

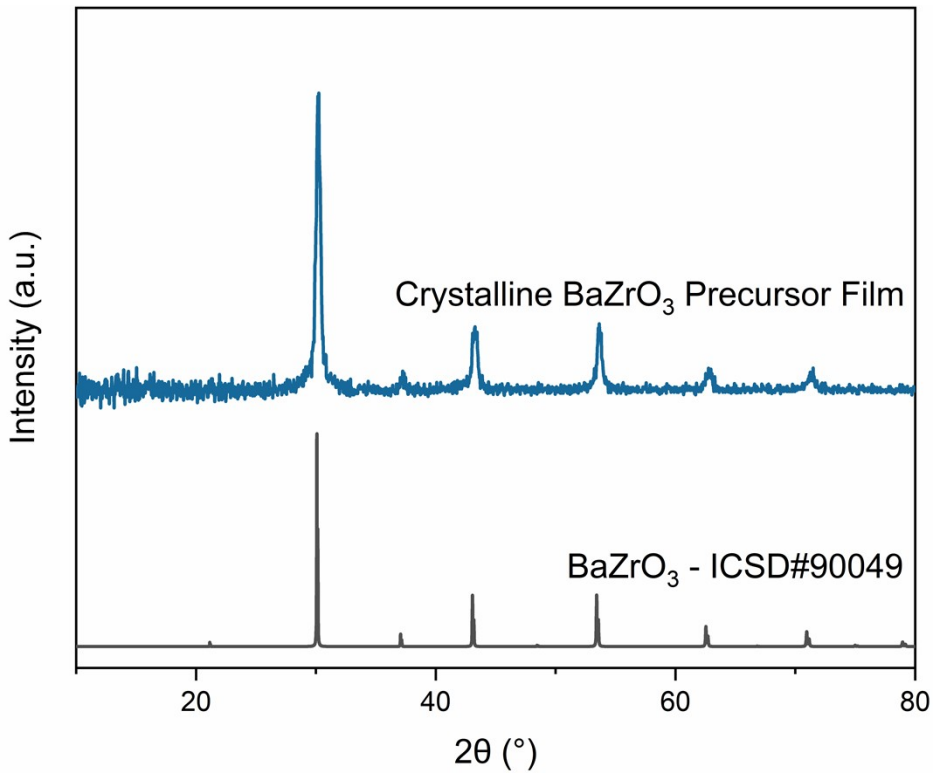

Figure S8. XRD pattern for the solution-processed $BaZrO_3$ precursor films used in this study.

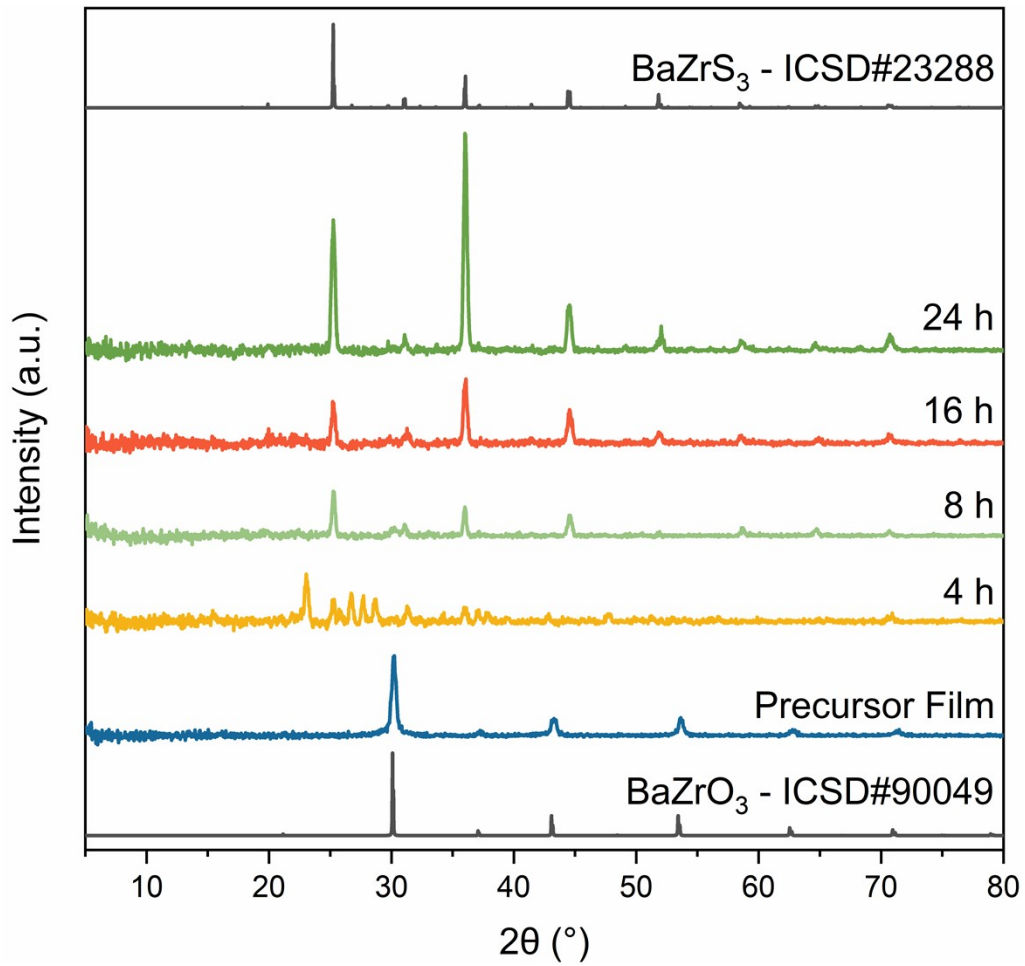

Figure S9. XRD patterns for a time study of the sulfurization of $BaZrO_3$ in the presence of HfH_2 and S powders to form $BaZrS_3$.

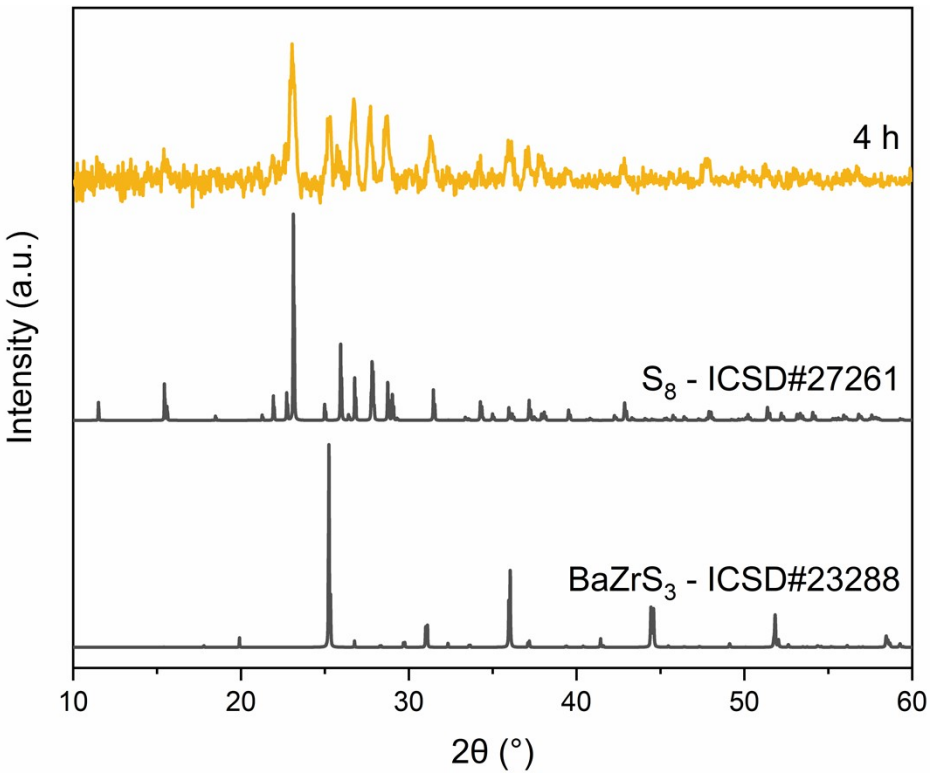

Figure S10. XRD patterns of the 4 h sample from the time study of the sulfurization of $BaZrO_3$. The peaks in this sample can be attributed to a combination of crystalline S_8 and $BaZrS_3$.

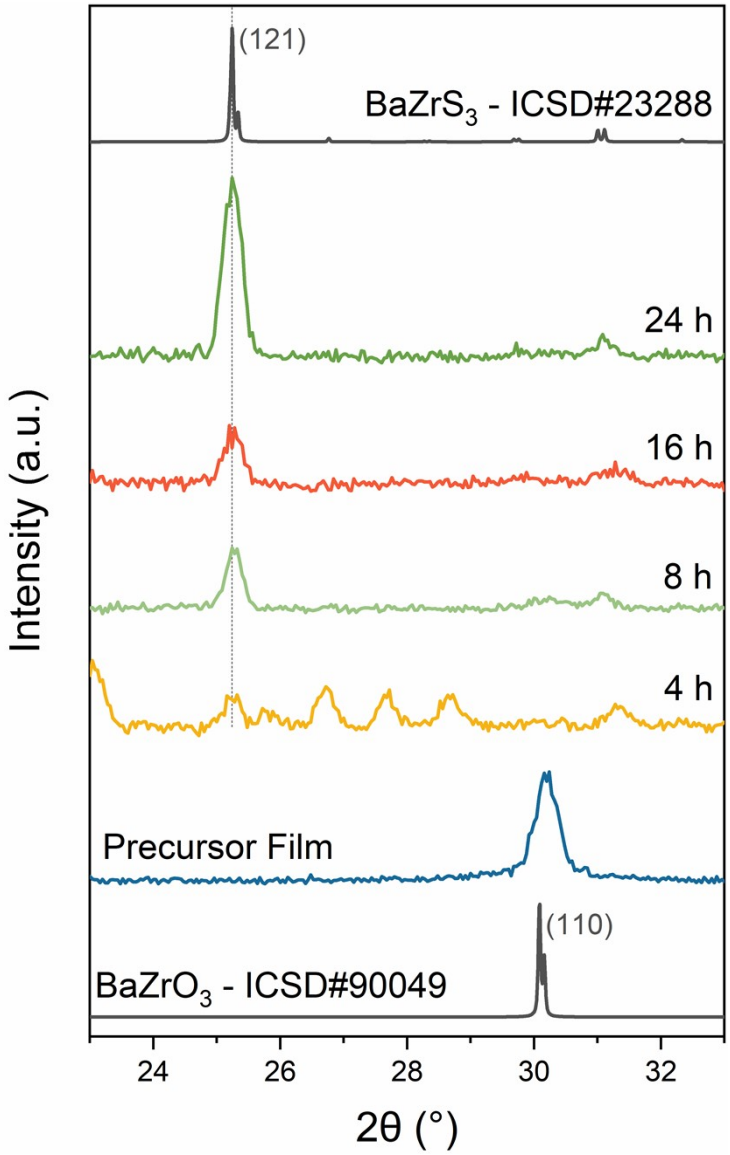

Figure S11. XRD patterns for the time study of the sulfurization of $BaZrO_3$ in the presence of HfH_2 and S powders to form $BaZrS_3$. Focused around the 110 peak of $BaZrO_3$ and the 121 peak of $BaZrS_3$ to show each form distinctly with no peak shift that would indicate a crystalline solid-state solution.

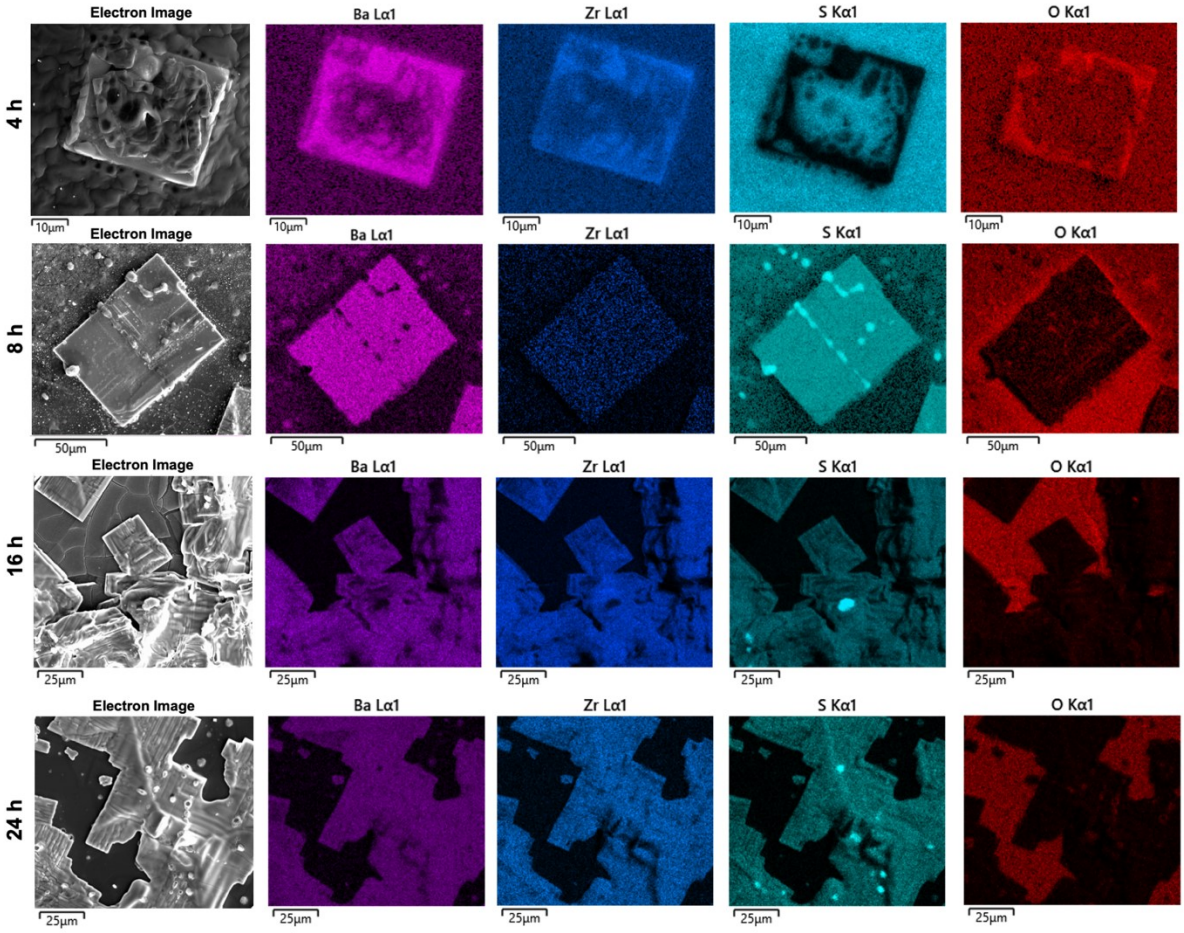

Figure S12. SEM/EDS images for the time study of the sulfurization of $BaZrO_3$ in the presence of HfH_2 and S powders to form $BaZrS_3$.

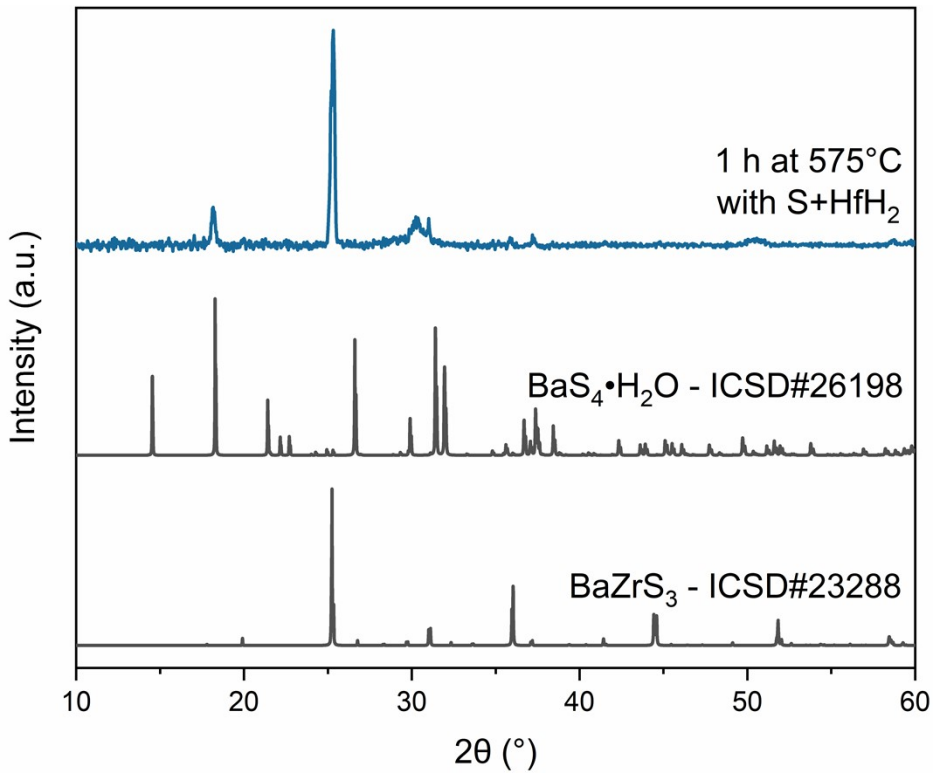

Figure S13. XRD pattern for a $BaZrO_3$ sample that was sulfurized for 1 h.

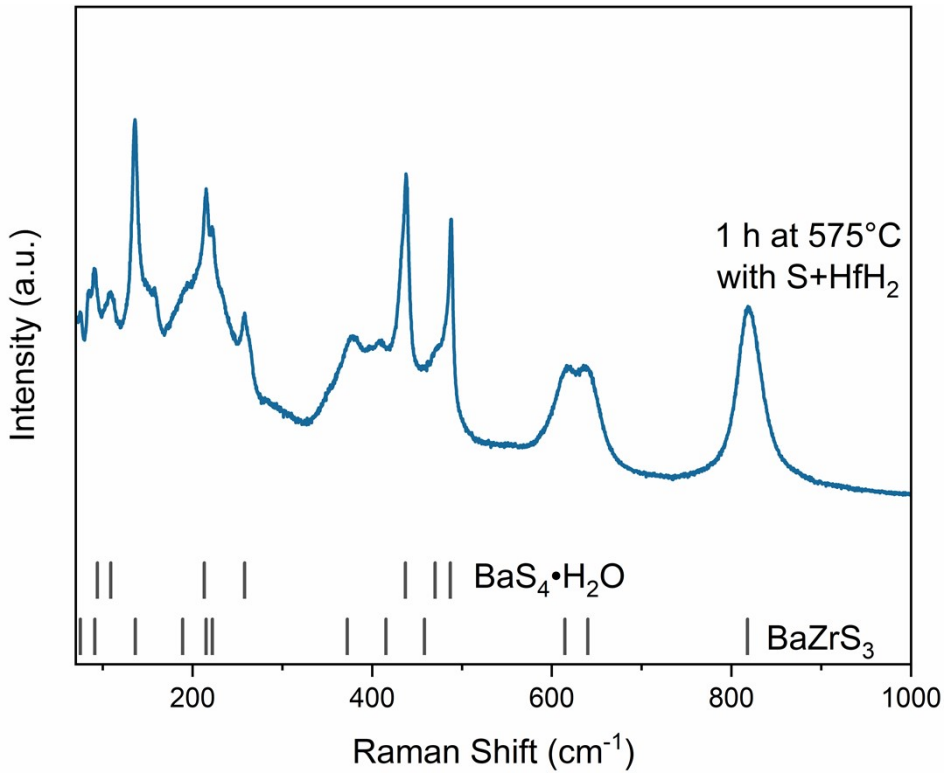

Figure S14. Raman spectrum for a $BaZrO_3$ sample that was sulfurized for 1 h. Reference Raman peak locations were identified by Pandey et al. and El Jaroudi et al.[11,12]

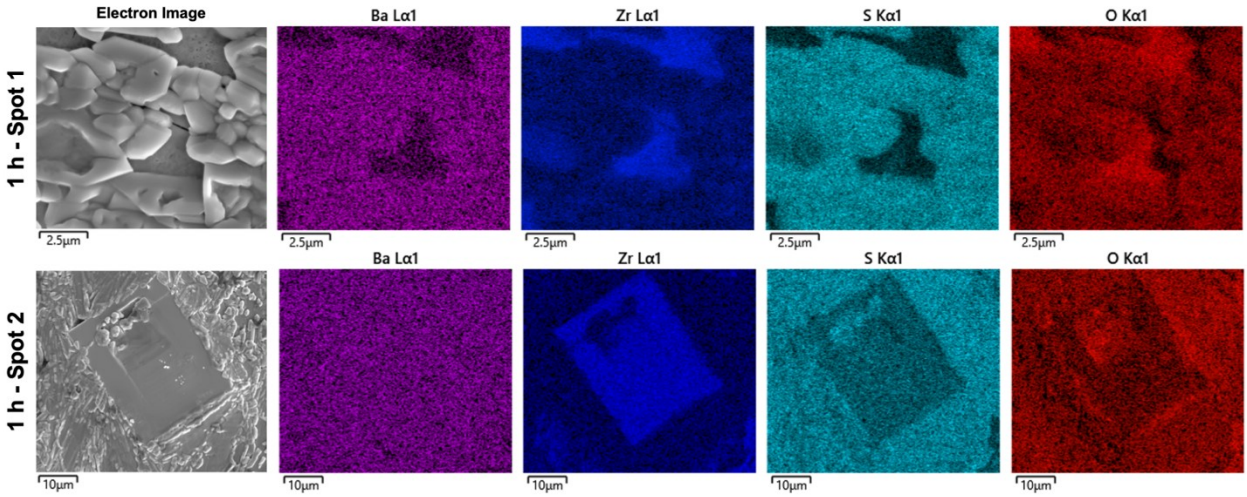

Figure S15. SEM/EDS images for two spots on a $BaZrO_3$ sample that was sulfurized for 1 h.

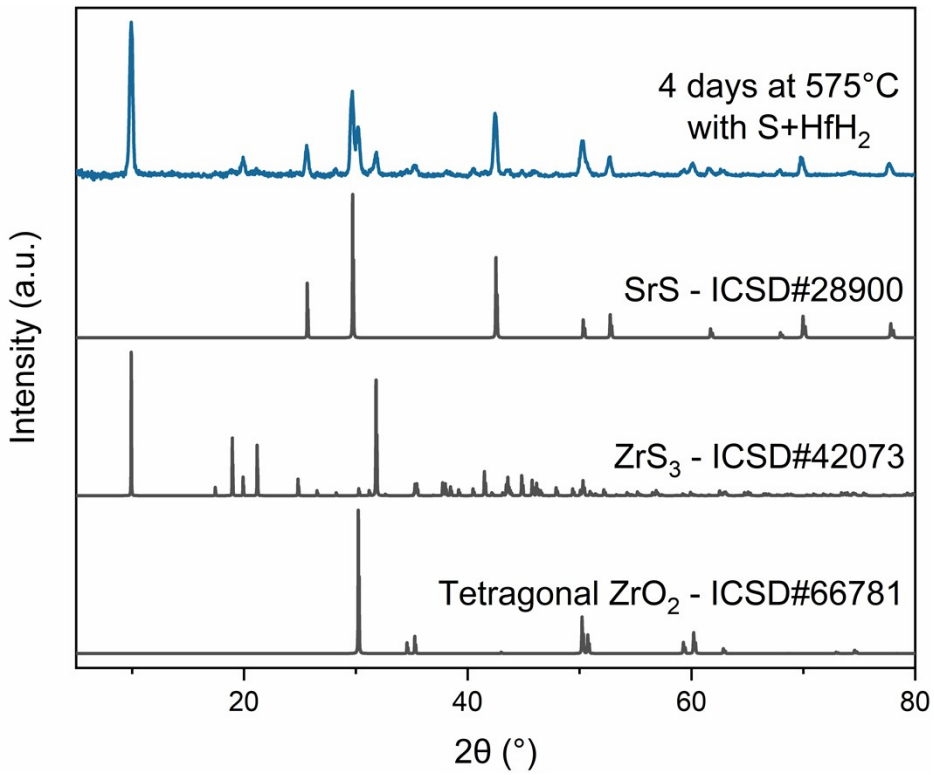

Figure S16. XRD pattern for the purchased $SrZrO_3$ powder that was heated in the presence of HfH_2 and S powders for 4 days at 575 °C. While sulfurization occurred, the binary sulfides were produced rather than the ternary $SrZrS_3$.

Supplementary Discussion 2: Application of this method to other chalcogenide perovskites

The power of this method lies in the thermodynamic driving force which strips the oxygen out of a metal oxide sample and converts it to a metal chalcogenide. However, the final form of that metal chalcogenide is determined by a variety of factors. For example, in the case where multiple metal sulfides are known (for example, ZrS_2 and ZrS_3), the metal sulfide that forms may depend on additional factors like the sulfur pressure. Additionally, whether the final metal chalcogenide that forms is crystalline or amorphous may depend on the temperature used.

When more complicated multinary metal oxide samples are chalcogenized, there are more possible outcomes that need to be considered. An example of this is shown above (Figure S12). While heating a $SrZrO_3$ sample in the presence of HfH_2+S can sulfurize the oxide perovskite, at these temperatures a mixture of binary metal sulfides is produced rather than the ternary $SrZrS_3$. This is an obvious difference compared to $BaZrO_3$/$BaZrS_3$. One possible explanation for this is the availability of a liquid barium polysulfide at temperatures above 525 °C. Barium polysulfides have recently been noted as a liquid flux that is capable in aiding the reaction of binary barium and zirconium sulfides to make $BaZrS_3$.[13,14] On the other hand, no liquid strontium polysulfides are known in this temperature range.

In applying similar methods to other chalcogenide perovskites, consideration should be given to the ability of the binary chalcogenides to form the ternary perovskites. For other barium- and sulfur-containing perovskites ($BaHfS_3$), the same barium polysulfide flux may allow for this method to be used with temperatures below 600 °C. However, for other systems higher temperatures may still be required or a different liquid flux may need to be introduced.

References

1 J. R. Rumble Jr., D. R. Lide and T. J. Bruno, Eds., *CRC Handbook of Chemistry and Physics*, CRC Press, Boca Raton, RL, 98th edn., 2017.

2 P. L. Brown, E. Curti and B. Grambow, *Chemical Thermodynamics of Zirconium*, OECD Nuclear Energy Agency, 1st edn., 2005.

3 K. C. Mills, *Thermodynamic Data for Inorganic Sulphides, Selenides and Tellurides*, The Butterworth Group, London, 1974.

4 C. L. Yaws, *Yaws Handbook of Thermodynamic Properties for Hydrocarbons and Chemicals*, Gulf Publishing Company, 2007.

5 H. Kopp, *Philos. Trans. R. Soc. London*, 1865, **155**, 71–202.

6 J. Leitner, P. Voňka, D. Sedmidubsky and P. Svoboda, *Thermochim. Acta*, 2010, **497**, 7–13.

7 R. Kresse, in *Metal Foams and Porous Metal Structures*, eds. J. Banhart, M. F. Ashby and N. A. Fleck, 1999, p. 109.

8 J. W. Turnley, K. Catherine Vincent, A. A. Pradhan, I. Panicker, R. Swope, M. C. Uible, S. C. Bart and R. Agrawal, *J. Am. Chem. Soc.*, 2022, **144**, 18234–18239.

9 T. Gupta, D. Ghoshal, A. Yoshimura, S. Basu, P. K. Chow, A. S. Lakhnot, J. Pandey, J. M. Warrender, H. Efstathiadis, A. Soni, E. Osei-Agyemang, G. Balasubramanian, S. Zhang, S. F. Shi, T. M. Lu, V. Meunier and N. Koratkar, *Adv. Funct. Mater.*, 2020, **30**, 2001387.

10 T. C. Peng, *J. Phys. Chem.*, 1974, **78**, 634–638.

11 J. Pandey, D. Ghoshal, D. Dey, T. Gupta, A. Taraphder, N. Koratkar and A. Soni, *Phys. Rev. B*, 2020, **102**, 205308.

12 O. El Jaroudi, E. Picquenard, A. Demortier, J.-P. Lelieur, J. Corset, C. Doukkali, D. De Physique, B. P. 20 and E. Jadida, *Inorg. Chem.*, 2000, **39**, 2593–2603.
13 K. C. Vincent, S. Agarwal, J. W. Turnley and R. Agrawal, *Adv. Energy Sustain. Res.*, 2023, **4**, 2300010.
14 R. Yang, J. Nelson, C. Fai, H. Arif Yetkin, C. Werner, M. Tervil, A. D. Jess, P. J. Dale and C. J. Hages, *Chem. Mater.*, 2023, **35**, 4743–4750.